Friederike Herrmann, Bernhard Jochim, Patrick Oßwald, Liming Cai, Heinz Pitsch and Katharina Kohse-Höinghaus, *Experimental and numerical low-temperature oxidation study of ethanol and dimethyl ether*, Combustion and Flame, **161** (2014) 384-397.

The original publication is available at www.elsevier.com

http://dx.doi.org/10.1016/j.combustflame.2013.09.014

Experimental and numerical low-temperature oxidation study of ethanol and dimethyl ether

F. Herrmann[1†], B. Jochim[2†], P. Oßwald[3], L. Cai[2], H. Pitsch[2*], K. Kohse-Höinghaus[1*]

[1] Department of Chemistry, Bielefeld University, Germany, Universitätsstraße 25, D-33615 Bielefeld, Germany

[2] Institute for Combustion Technology, Aachen University, Germany, Templergraben 64, D-52056 Aachen, Germany

[3] German Aerospace Center (DLR), Institute of Combustion Technology, Pfaffenwaldring 38-40, D-70569 Stuttgart, Germany

[†] They both contributed equally to this work.

[*] Corresponding authors: K. Kohse-Höinghaus, H. Pitsch
kkh@uni-bielefeld.de, +49 521 106 2052
h.pitsch@itv.rwth-aachen.de, +49 241 80 94608

revised manuscript for

Combustion and Flame

Abstract

Low-temperature combustion (LTC) receives increasing attention because of its potential to reduce NO_x and soot emissions. For the application of this strategy in practical systems such as internal combustion engines and gas turbines, the fundamental chemical reactions involved must be understood in detail. To this end, reliable experimental data are needed including quantitative speciation to assist further development of reaction mechanisms and their reduction for practical applications.

The present study focuses on the investigation of low-temperature oxidation of ethanol and dimethyl ether (DME) under identical conditions in an atmospheric-pressure laminar flow reactor. The gas composition was analyzed by time-of-flight (TOF) mass spectrometry. This technique allows detection of all species simultaneously within the investigated temperature regime. Three different equivalence ratios of ϕ=0.8, 1.0, and 1.2 were studied in a wide, highly-resolved temperature range from 400 to 1200 K, and quantitative species mole fraction profiles have been determined.

The experiments were accompanied by numerical simulations. Their results clearly show the expected different low-temperature oxidation behavior of both fuels, with a distinct negative temperature coefficient (NTC) region only observable for DME. With detailed species information including intermediates, differences of the kinetics for both fuels are discussed. Small modifications of the mechanisms served to identify sensitivities in the model. The experimental results may assist in the improvement of kinetic schemes and their reduction.

Keywords: time-of-flight mass spectrometry, dimethyl ether oxidation, ethanol oxidation, low-temperature oxidation, laminar flow reactor, kinetic modeling

1. Introduction

For a transformation of the global energy system towards increasing sustainability, it is desirable to improve conventional or to design novel combustion processes, while at the same time, environmentally-friendly fuels and routes to their production should be identified. Future combustion processes must feature substantially reduced pollutant emissions while maintaining high efficiency. A promising concept in that respect is low-temperature combustion (LTC). The LTC regime can be realized, for example, by high dilution of the fuel-oxidizer mixture through exhaust gas recirculation [1]. The low-temperature behavior is

important for homogeneous charge compression ignition (HCCI) engines [2-5], characterized by low soot and low NO_x emissions [6-10]. Combustion at low temperatures may feature different reaction pathways from those occurring in the common high-temperature combustion regime. Low-temperature kinetics could lead to combustion instabilities, and appropriate control strategies may be needed [11].

The reaction schemes for many fuels in the low-temperature regime have recently been reviewed by Battin-Leclerc [12] and Zádor et al. [13]. However, detailed kinetic studies for the low-temperature regime are scarce, and the examination of reaction mechanisms for combustion in a highly diluted regime is of particular importance. Ethanol as an established alternative fuel and its isomer dimethyl ether (DME) are interesting targets for an in-depth analysis under such conditions.

A significant number of studies exists on both ethanol and DME combustion. Ethanol combustion reactions have been investigated experimentally and in mechanistic studies [14-18,19], with the mechanism of Cancino et al. [17] as the only ethanol oxidation mechanism in the intermediate-temperature regime. The thermal decomposition of ethanol in a flow reactor was investigated in an early study by Rotzoll [20] and, more recently, by Li et al. [21]. Ethanol combustion was studied in low-pressure flames [18,22-26], and ethanol oxidation was investigated at 1100 K in a flow reactor by Norton and Dryer [27]. Haas et al. [28] have investigated the low- and intermediate-temperature oxidation of ethanol in a flow reactor under knock-relevant conditions, while Alzueta et al. [29] have addressed the influence of NO on ethanol oxidation. More recently, Leplat et al. [23] and Dagaut et al. [30] have investigated the oxidation of ethanol in a jet-stirred reactor (JSR) at atmospheric and high pressure in the ranges of 890-1250 K and 770-1220 K, respectively. Although Frassoldati et al. [19] have modeled low-pressure propene-oxygen-argon flames blended with DME or ethanol at higher temperatures, a comparative study of the low-temperature chemistry of the isomeric fuels ethanol and DME, especially in the regime below ~800 K, is still lacking.

Mechanisms for oxidation and pyrolysis of DME in the low- and high-temperature regimes have been reported in [31-34]. Hidaka et al. [35] and Sivaramakrishan et al. [36] investigated the pyrolysis of DME, while Pfahl et al. [37] studied its autoignition. A wide range of combustion conditions for DME was addressed in several flame experiments [26,38-43]. Also, DME oxidation was investigated by Dagaut et al. [44,45] in a JSR, and its thermal decomposition and oxidation in a flow reactor were studied by Fischer, Curran and the group

of Dryer et al. [31-33]. Moreover, Liu et al. [46] and Alzueta et al. [47] have investigated the influence of NO on DME oxidation. Species concentrations in previous work have commonly been determined by Fourier-transform infrared (FT-IR) spectroscopy or online gas chromatography (GC). Mass spectrometric detection of species in DME oxidation in a flow reactor has only been used by Guo et al. [48] and in our own work [49].

Here, we report quantitative mole fractions of reactants, products and intermediates for both DME and ethanol oxidation, using simultaneous mass spectrometric detection for all species. A laminar flow reactor was coupled to an electron ionization (EI) time-of-flight (TOF) mass spectrometer and used for a systematic study of the low-temperature oxidation for the two C_2H_6O-isomers over a wide temperature range of 400-1180 K at equivalence ratios of ϕ=0.8, 1.0, and 1.2. With online detection of the complete stable species pool, a superior temperature resolution was achieved through continuous ramping of the reactor temperature. Identical conditions were chosen for both fuels so that a direct comparison is feasible. A major aspect of our present paper is to report the experimental data for the interesting low-temperature oxidation regime. Modeling was performed in addition for a better understanding of the chemistry in this system, but not with an aim to develop a new model. An analysis of the low-temperature combustion chemistry with mechanisms available in the literature was performed to elucidate details of the reaction pathways. Minor changes in the kinetic models served to emphasize sensitive reactions in the established mechanisms.

2. Experiment

Systematic studies of the oxidation of ethanol and DME were performed under near-identical conditions for both fuels. The experimental setup was described in detail in [49], and thus only details relevant to this study are given here. An overview of the setup is given in Fig. 1. The experimental results for DME oxidation have been previously reported in [49] without a kinetic model.

2.1 Experimental conditions

For both fuels, the exhaust gas composition was determined as a function of the reactor temperature. To achieve high temperature resolution, i. e. measurements at a multitude of individual temperature values, the entire reactor length was heated with applying a constant ramp of 0.16 K/s generated by a temperature controller (Horst HT60). By this procedure, mass spectra were obtained in steps of 8.7 K. The temperature range for DME started from

1115 K and ended at 410 K, and for ethanol from 1178 K to 421 K. The reactor wall temperature was observed and controlled with a Ni-Cr/Ni thermocouple positioned at 350 mm downstream of the beginning of the heated reactor section (see Fig. 1a) and inserted between the reactor wall and the heating tape. Due to small inhomogeneities across the tube, the absolute temperature error was higher (<5%) than the stated uncertainty of the thermocouple (<0.4%). The gases were fed premixed to the flow reactor with 97% argon dilution. Under these highly diluted conditions, self-sustaining combustion is suppressed. The flow rates of the gases were regulated by calibrated mass flow controllers. The flow velocity at 400 K was 0.25 m/s, resulting in laminar flow conditions. Table 1 presents the gas flow rates (in g/min) for both fuels and for the investigated stoichiometry series (ϕ=0.8, 1.0, 1.2). For comparison, temperature profiles along the centerline of the reactor were measured for different isothermal reactor wall temperatures with a non-reactive isothermal argon gas flow at 0.5 slm (Fig. 1b).

2.2 Vaporizer system for ethanol fuel

Liquid ethanol flow rates of 8.2-11.2 µl/min were provided with a vaporizer system, shown schematically in Fig. 1a. The system consists of a syringe pump (Protea, PM-1000) suitable for these small feeding rates. The liquid fuel was fed through a 55.5 mm-long stainless steel tube into the vaporizer chamber, the main length of which (51.5 mm) extended into this chamber. The end of the tube was crimped to provide a small drop size of the liquid fuel and to improve the vaporization.

The vaporizer chamber with an inner diameter of 4 mm and a length of 117 mm was heated electrically by a heating tape (Horst, HSQ and HT60 control) and the outer wall temperature, controlled by a Ni-Cr/Ni thermocouple, was kept constant at 393 K±1.6 K. At a position of 10 mm from the chamber inlet, a preheated argon flow (88% of the main argon flow rate) was introduced to pick up the vaporized ethanol in the gas stream into the reactor inlet. The pressure inside the vaporizer chamber and the flow reactor was controlled via a valve and set to 970 mbar. The preheated argon flow and the pressure control were instrumental in assuring a steady ethanol flow.

2.3 Species detection

Since the coupling of the reactor to the mass spectrometer was described previously [49], only some details are given here. Species detection was performed at the reactor outlet using an EI-

TOF mass spectrometer. A gaseous sample was taken via a needle valve at the reactor outlet and guided with a 110 cm transfer line to the ion source. With low pressure behind the valve (<1 mbar), significant delay between reactor outlet and detection was avoided. However, although the mass spectrometric method allows simultaneous detection of almost all species, only stable species could be detected with this sampling technique. Ionization was performed at an electron energy of 20 eV so that it was necessary to consider fragmentation of the fuels. The relevant fragmentation patterns were measured from cold gas samples and used for a rigorous fragmentation correction. For the detection of species in the oxidation of both fuels, 10^6 sweeps were averaged, leading to a total measurement time of 52 s/spectrum. The mass resolution of R=1600 allowed to determine the elemental composition so that C_2H_4 could be separated from CO and C_2H_6 from CH_2O.

2.4 Data evaluation

The calibration procedure used in this study was adapted from [50-52] and described in detail in [49]. To follow the discussion of the results, a brief description is included. The integrated ion signal S_i of a species i is linked to its mole fraction x, by comparison to a signal of a reference species R.

$$\frac{S_i}{S_R} = \frac{x_i}{x_R} \cdot k_{i/R}(E) \qquad (1)$$

The calibration factor $k_{i/R}$ (E) is energy-dependent and constituted from numerous experimental constants. In this study, Ar was used as the reference species and its mole fraction was assumed as constant because of the high dilution of reactants. To determine the calibration factors for the major species (fuel, O_2, CO_2, H_2O, CO, and H_2), an internal calibration procedure was used as described previously in [49]. The calibration factors for the intermediates were established by the simulation of the respective signal (see Supplement of [49] for details); ethane was calibrated directly with a calibration mixture.

Uncertainties resulting from this approach consist of two different components. The first one depends on the error in the mole fraction of argon, which is negligible, however, because argon is the main constituent (97%) of the gas mixture. The second error source is caused by uncertainties in the cross sections; typically less than a factor of 2 for minor species and <30% for major species. However, relative trends for a specific species can be compared with significantly higher accuracy, i.e. within 20% error.

3. Kinetic modeling

The oxidation of both fuels under all conditions was simulated with a flow reactor model using different kinetic mechanisms from the literature, including some improvements suggested in the present work.

3.1 Numerical model

The simulations were performed with the constant pressure homogeneous reactor model of the FlameMaster program [53]. The assumptions for treating a laminar flow reactor as a homogeneous reactor problem are discussed in detail in Wada et al. [54]. In this paper, it is shown that through an analytic solution for oxidation of DME, the system of equations describing the two-dimensional steady flow in a laminar flow reactor can be reduced to a set of ordinary differential equations. This approach substantially simplifies the numerical model and significantly reduces the computation time. A conversion of space to time is performed to allow for the interpretation of experimental data. The resulting set of governing equations is as follows:

$$\frac{\mathrm{dY}_i}{\mathrm{dt}} = -\frac{\omega_i}{\rho} \tag{2},$$

$$\frac{\mathrm{dT}}{\mathrm{dt}} = -\frac{1}{\rho \cdot c_p} \sum_{\mathrm{i}=1}^{\mathrm{ns}} \omega_{\mathrm{i}} h_i - \frac{\dot{Q}_{Wall}}{c_p} \tag{3},$$

$$\dot{Q}_{Wall} = A_{Wall} \cdot h_{Wall} (T - T_h) \tag{4}.$$

Here, Y_i is the mass fraction of species *i*, *t* is the time, ω_i the chemical source term of species *i*, ρ the density, *T* the temperature, c_p the heat capacity at constant pressure, h_i the enthalpy of species *i*, *ns* is the number of species. The wall heat transfer $\dot{Q}_{wall}$ is assumed proportional to the difference in fluid and heating temperature, where A_{Wall} is the wall area and T_h the heating temperature. The heat transfer coefficient h_{Wall} was adjusted so that the experimental gas temperature was matched for a non-reactive but heated case. Data were available for the heating temperatures T_h=1100 K, 973 K and 576 K. The heat transfer coefficient h_{Wall} is always of the order of magnitude of 1W m^{-2} and was set as temperature-dependent over the axial direction of the flow reactor to account for the changing gas temperature T_{gas}. For heating temperatures in between and beyond the available data sets, the wall heat transfer was

linearly interpolated. The axial position *l* was calculated depending on the simulation time and the fluid velocity for every numerical time step. A comparison of simulation and experiment for the non-reacting cases is shown in Fig. 1b.

3.2 Kinetic mechanisms

The chemical source term was accounted for by detailed kinetic mechanisms. For each of the two fuels, two different mechanisms were applied.

3.2.1 Ethanol

The mechanisms of Cancino et al. [17] ("*Cancino* mechanism") and Zhao et al. [34] ("*Zhao* mechanism") were chosen for the simulation of the ethanol oxidation experiments. The *Cancino* mechanism comprises 136 species and 1349 elementary reactions. It was developed for thermal oxidation of ethanol at intermediate temperatures starting from the high-temperature ethanol mechanism by Marinov [14] and the C_3 oxidation chemistry of Konnov [55]. The mechanism was validated against ignition delay times from shock tube experiments for a range of equivalence ratios of 0.25-2.0, pressures of 2.0-50 bar, and temperatures of 650-1600 K. The numerical results were also compared to global relations for ignition delay times obtained by multiple regression analysis of experimental data by Dunphy and Simmie [56]. Finally, a sensitivity analysis was carried out with respect to temperature and OH, H_2O_2 and C_2H_5O concentrations revealing the importance of several reactions describing hydrogen-atom abstraction from ethanol by the hydroperoxy radical (HO_2) [17].

The *Zhao* mechanism was originally developed for DME oxidation. The reaction scheme is based on a H_2/C_1-C_2 submodel which can also describe ethanol oxidation [34]. The detailed ethanol subset [57] was developed in a hierarchical manner and tested against a wide range of experimental results obtained from premixed laminar flames, shock tubes, and flow reactors. Simulations with this mechanism were successful in predicting the structure of counterflow diffusion and partially premixed flames [58] and were also found in good agreement with ignition delay times [59] and laminar burning velocity results.

3.2.2 DME

The DME experiments were modeled with the kinetic mechanisms developed by Curran et al. [32] and Fischer et al. [33] as well as with that by Zhao et al. [34]. The former was based on a mechanism by Curran et al. [31] consisting of 78 chemical species and 336 chemical

reactions. It was validated against experimental data over a wide range of conditions, including JSR results for 1-10 bar, 800-1300 K and equivalence ratios from 0.2 to 2.5 [45] as well as shock tube results for stoichiometric conditions at 13 bar and 40 bar and 650-1300 K [37]. Additional experiments in an atmospheric-pressure flow reactor at 1085 K and in a variable-pressure flow reactor (VPFR) at 2.5 bar and 1118 K with equivalence ratios varying between 0.32 and 3.4 led to a revised model for the high-temperature pyrolysis and oxidation of DME [33]. These experiments were conducted at turbulent conditions where the fuel was diluted by large amounts of preheated nitrogen. Low- to intermediate-temperature experiments in the VPFR ranging from 550-850 K, 12-18 bar and equivalence ratios from 0.7 to 4.2 showed formic acid as a major intermediate. Because these observations could not be reproduced with the original DME mechanism [31], formic acid chemistry was included in the updated version [32]. The combined version of Curran et al. [32] and Fischer et al. [33] (here named "*CF* mechanism"), representing high- and low-temperature combustion of DME, comprises 82 species and 351 reactions.

The other mechanism used was the more recent one of Zhao et al. [34] already mentioned for ethanol oxidation above. Applying a hierarchical methodology, these authors had developed a high-temperature model including new unimolecular decomposition parameters and recent kinetic and thermochemical data for small molecules and radicals. In comparison to the mechanism by Fischer et al. [33], their updated decomposition rate coefficient obtained from RRKM/master equation calculations differs significantly. In addition to the aforementioned data, the high-temperature model by Zhao et al. [34] was validated against DME pyrolysis experiments in a VPFR at 980 K and 10 bar, a significantly higher pressure compared to previous validation data. The model was also successfully tested against low-pressure burner-stabilized species profiles and laminar flame data for DME/methane mixtures. In the full Zhao et al. [34] mechanism, applied for both ethanol and DME, the high-temperature part was combined with a modified oxidation model of Curran et al. [32] leading to 55 species and 290 reactions.

Schofield [61] suggests to evaluate relative molar response factors for carbon detection in a flame ionization detector (FID). For the conditions of the FID flame, the response exhibits a strict proportionality to total carbon number, except for molecules where parts of the carbon content is masked e.g. by an oxygenated moiety. The fraction of masked carbon depends on the specific structure, i.e. one carbon atom will be masked by the ether moiety and 0.5

carbons by a primary OH group. These fractions are indeed correctly captured with the Zhao et al. [34] mechanism for both fuels., i.e. the primary fuel destruction pathways produce one oxygenated (invisible for the FID) carbon fragment per DME molecule and ~0.5 per molecule ethanol respectively [62]. The latter is due to the abstraction of the α- and hydroxyl-hydrogens; both pathways produce CO and a respective C1 compound.

Experimental temperature profiles along the reactor axis were available for stoichiometric DME oxidation at heating temperatures T_h =1100 K and T_h =576 K and are shown in Fig. 1c together with the simulations. The *Zhao* mechanism tends to predict slightly earlier ignition than in the experiment as seen in the data for T_h =1100 K. For the lower heating temperature T_h =576 K, the *Zhao* mechanism shows a small heat release at 440 mm reactor length, while the *CF* mechanism exhibits an even smaller increase at 520 mm. Overall, both mechanisms reproduce the experimental results very well, with a slightly better representation by the *CF* mechanism.

3.2.3 Modifications

Both kinetic mechanisms applied for DME oxidation showed noticeable differences when compared to the experimental results. Based on a detailed analysis, the mechanisms were thus carefully modified in some aspects. Table 2 summarizes the changes. Note that none of the applied modifications led to significant changes in the high temperature kinetics (Fig. 2b and d) of the respective mechanisms.

Measured and computed DME mole fractions at stoichiometric conditions are represented in Fig. 2a for the *CF* mechanism and in Fig. 2c for the *Zhao* mechanism. While the general trends are quite well represented, both simulations reveal some shortcomings. The *CF* mechanism overestimates the values around 820 K and predicts complete conversion at higher temperatures than seen in the experiment. The *Zhao* mechanism leads to distinct spikes in the profile near 800 K and a second one at higher temperature which required further investigation.

3.2.3.1 *CF* mechanism modifications

As mentioned above, Zhao et al. [34] updated the rate coefficient for unimolecular DME decomposition performing RRKM/master equation calculations leading to different parameter sets compared to the proposed values of Fischer et al. [33]. Because of the increasing

importance of such DME consumption reactions with temperature, the rate coefficients for the following three reactions were taken from the more recent *Zhao* mechanism:

$$CH_3OCH_3 + \dot{C}H_3 \rightarrow CH_3O\dot{C}H_2 + CH_4 \quad \text{(R5)},$$

$$CH_3O\dot{C}H_2 \rightarrow CH_2O + \dot{C}H_3 \quad \text{(R6)},$$

$$HO_2CH_2OCHO \rightarrow \dot{O}CH_2OCHO + \dot{O}H \quad \text{(R7)}.$$

The original and modified rate expressions are summarized in Table 2, and an Arrhenius diagram for the entire temperature range is available in Fig. S2 in the Supplemental Material.

It is interesting to note that a more recent kinetics study [63] suggests rate coefficients for R5 indicating that the original values of the CF mechanism are more appropriate. However, in the present study, the kinetic data for R5 as proposed by Zhao et al. [34] lead to the best agreement with experiments and are applied in the remainder of this work. Furthermore, it is found that despite the relatively high activation energy of R6 it has a significant influence on the results for heating temperatures between 750 and 1000 K.

The resulting simulations with the original ("*CF*") and modified ("*mod-CF*") kinetic mechanisms are given in Fig. 2a. The modified rate coefficients lead to a better agreement with the experimental data, including a reduced delay in the fuel decomposition at higher heating temperatures and a less significant overestimation of the maximum DME mole fraction. This improved behavior is also evident in Fig. 2b, which summarizes the main DME decomposition paths in terms of integrated, normalized reaction rates as a function of the heating temperature, obtained as follows: individual reaction rates were integrated over simulation time, i.e. reactor length. Two sums of integrated reaction rates were then computed, one for all production rates, $\Omega_P = \sum_i \omega_{i,P}$, and the second for all consumption rates, $\Omega_C = \sum_i \omega_{i,C}$. Individual integrated production rates were normalized by Ω_P, and for consumption reactions, by $-\Omega_C$. Thus, a value of zero indicates no contribution while a value of 1 (for production) or -1 (for consumption) means that only this reaction is relevant. In addition to the contribution of R5, those of several further reactions are also displayed:

$$CH_3OCH_3 \rightarrow \dot{C}H_3 + CH_3\dot{O} \quad \text{(R8)},$$

$$CH_3OCH_3 + \dot{O}H \rightarrow CH_3O\dot{C}H_2 + H_2O \quad \text{(R9)},$$

$$CH_3OCH_3 + \dot{H} \rightarrow CH_3O\dot{C}H_2 + H_2 \quad \text{(R10)},$$

$$CH_3OCH_3 + O_2 \rightarrow CH_3O\dot{C}H_2 + H\dot{O}_2 \quad \text{(R11)}.$$

In the temperature region below 600 K, DME is dominantly consumed by R11 and R9 (see Fig. 2), while above 1000 K, an increasing contribution of R8 is observed. This is in line with the common understanding of DME oxidation that the main abstraction partners in this region are O_2 and OH, while the pyrolysis processes are primarily observed at high temperatures.

At intermediate temperatures, reactions of DME with OH (R9), CH_3 (R5) and H (R10) are predominant. Three distinct regimes can be distinguished. In the NTC regime, between 600 and 800 K, R9 governs the DME oxidation. At higher temperatures from 800 up to 975 K, R5 has the largest contribution while for the temperatures above 975 K, all three reactions are of similar importance. The rate expression modifications have their largest impact above 800 K. As expected, the importance of R5 is increased. Distinct changes are seen for 800-975 K, and interestingly, even trends have changed for higher temperatures. Here, R5 makes a larger contribution than R10 and additionally surpasses R9 at 1000 K. The increased contribution of R5 obviously accelerates the decomposition of DME in the NTC regime as well as at higher temperatures, a result which agrees well with the experiment.

3.2.3.2 *Zhao* mechanism modifications

A stronger emphasis was put on the modification of the *Zhao* mechanism, especially because of the observed spikes near 800 K. To better understand the reason for this spikes, such modifications were necessary. Additionally these small changes in the kinetic model highlight the sensitivities in the established chemical mechanism. Inspection of the mechanism revealed that the complete path of the methyldioxy radical (CH_3O_2) was not included. As a consequence, four reactions were added from the *CF* mechanism. Moreover, the pressure dependence of the CH_3O reaction with a third body was implemented:

$$CH_3\dot{O}_2 + M \rightarrow \dot{C}H_3 + O_2 + M \quad \text{(R12)},$$

$$CH_3\dot{O}_2 + CH_2O \rightarrow CH_3\dot{O} + OH + HC\dot{O} \quad \text{(R13)},$$

$$CH_3\dot{O}_2 + \dot{C}H_3 \rightarrow CH_3\dot{O} + CH_3\dot{O} \quad \text{(R14)},$$

$$CH_3OCH_3 + CH_3\dot{O}_2 \rightarrow CH_3O\dot{C}H_2 + \dot{O}H + CH_3\dot{O} \quad \text{(R15)},$$

$$CH_3\dot{O} + M \rightarrow CH_2O + \dot{H} + M \quad \text{(R16)}.$$

The modified rate expressions (including the original one for R16) are summarized in Table 3; they were directly taken from the *CF* mechanism, except for two changes. Data for R14 were taken from the more recent publication of Petersen at al. [66] and the species CH_3O_2H was omitted from the mechanism, because the reaction $CH_3O_2H \rightarrow CH_3\dot{O} + \dot{O}H$ is very fast.

Note that CH_3O_2 originates from O_2 addition to methyl. The results with the original ("*Zhao*") and modified *Zhao* mechanism ("*mod-Zhao*") are shown in Fig. 2c, demonstrating much better agreement of the latter with the experiment.

Again, Fig. 2d shows the integrated and normalized reaction rates for the predominant DME decomposition reactions. The same paths are involved as for the *CF* mechanism and the general characteristics are similar, with dominant influence of R11 and R9 at low temperatures and increasing influence of DME pyrolysis at higher temperatures (R8). A distinct NTC regime is observed at intermediate temperatures, where the original model shows the aforementioned spikes near 800 K while the modified one does not. The influence of the modifications above 750 K can be seen also in the profiles for R5, R9, and R10. The improvement between experiment and simulation achieved with the *mod-Zhao* mechanism for all three stoichiometries emphasizes the importance of the CH_3O_2 chemistry at the investigated conditions.

4. Results and discussion

In the following, ethanol and DME oxidation under the same conditions will be compared presenting results from experiments and simulation. While the experimental data for DME was already published [49] without kinetic modeling, model results for these conditions as well as the ethanol results from both experiment and modeling are reported here for the first time.

As a general result, the detected species pool for both fuels at each stoichiometry is similar, including fuel and O_2 at low temperature, the final oxidation products H_2O and CO_2 at high temperatures as well as the typical combustion intermediates CO, H_2, CH_4, C_2H_4, C_2H_2, C_2H_6, and CH_2O. For ethanol, C_2H_4O was detected, and for DME as the fuel, $C_2H_4O_2$ and CH_2O_2 were observed. Within the available resolution of the EI-TOF spectrometer, the signal of CH_2O_2 could not be reliably quantified, however, because of interference with the signal of DME as the fuel at the same nominal mass. H_2O_2 was not detected within the detection limit of $\sim 10^{-5}$ although the models predict mole fractions in the range of $6\text{-}8\times10^{-4}$. Potentially, fragmentation due to the high ionization energy, the length of the transfer line or neglected wall effects may have contributed to H_2O_2 loss before detection. Furthermore, species with more than two carbon atoms, including hydrocarbons or aldehydes, were not observed at any stoichiometry within this detection limit. To facilitate comparison, only the species profiles

for ϕ= 1.0 are shown in the following figures, while the discussion includes reference also to the cases with ϕ=0.8 and 1.2; the respective figures for the lean and rich cases are presented in the Supplemental Material.

4.1 Ethanol oxidation

4.1.1 Major species

Mole fraction profiles as a function of temperature for the major species, including the fuel (ethanol), O_2, H_2, CO, H_2O, and CO_2, are presented in Fig. 3 for ϕ=1.0 and in Fig. S3 for the lean and rich conditions; experimental results are given together with the simulations using the *Cancino* and *Zhao* mechanisms. Equilibrium values for the different mixtures calculated for *T*=1100 K with the Gaseq program [68] are included in these diagrams; they are offset to T>1200 K to avoid interference with measured data points. In general, most trends are reasonably well captured by both models, including the equilibrium mole fractions, with pronounced deviations between experiment and model especially noted for H_2 at ϕ=1.0 and 0.8, however. Best overall agreement is seen for the fuel-rich condition.

Some aspects merit a more detailed discussion. In the profiles for ethanol and H_2O in Fig. 3a, the simulations with the *Zhao* mechanism show a non-negligible discrepancy of the ignition temperature, where the model shows an initial ethanol decrease at ~840 K, while distinct ethanol consumption is already observed in the experiment starting at <700 K. This temperature shift of ~140 K can be found in all species profiles. In the experiment, a gradual decrease is observed starting near 500 K and a more pronounced consumption around 800 K. It is known that heterogeneous dehydration reactions of ethanol can lead to its depletion already at low temperatures [28], which could be assumed to explain the observed discrepancy. However, the experimental behavior is very well captured by the *Cancino* mechanism which should be particularly suitable also for the intermediate temperature range and heterogeneous reactions don't seem to be of major influence here. According to a reaction flow analysis with this mechanism [17] for the stoichiometric condition, ethanol is primarily consumed in the relevant temperature range (i.e. 500-790 K for R17 and 500-680 K for R18) by the reactions:

$$C_2H_5OH + H\dot{O}_2 \rightarrow CH_3\dot{C}HOH + H_2O \quad \text{(R17)},$$

$$C_2H_5OH + CH_3\dot{O}_2 \rightarrow CH_3\dot{C}HOH + CH_3O_2H \quad \text{(R18)},$$

Increasing temperature in this range leads to increasing HO_2 production via reaction of the resulting CH_3CHOH radical with O_2; furthermore, the recombination of two HO_2 molecules to O_2 and H_2O_2 becomes more important. R18 ceases to be of major importance near 680 K. Above ~800 K, CH_3CHOH is mainly consumed to produce CH_3 and CH_2O:

$$CH_3\dot{C}HOH + M \rightarrow \dot{C}H_3 + CH_2O + M \quad \text{(R19)}.$$

Somewhat similar trends were observed by Haas et al. [28] and Leplat et al. [23], for different experimental conditions, however. The trends in the ethanol profile, i.e. a gradual consumption in the lower temperature range up to about 800 K, followed by a more pronounced decrease of the mole fraction above this temperature, are also reflected in the profiles of major and some intermediate species in Figs. 3-5 and S3-S5. These trends are clearly seen in the prediction with the *Cancino* mechanism which shows a somewhat more pronounced step in the profiles, however.

The mole fraction profile of O_2 in Fig. 3b also exhibits this step between 650 K and 790 K already discussed for the fuel profile. In addition, it shows an interesting behavior in the range of ~800-985 K. First, gradual consumption occurs up to ~810 K, followed by a steeper decrease of the mole fraction up to ~950 K, where an additional step is observed in the experimental profile, with a more rapid consumption up to ~985 K. This characteristic shape, namely a change of slope in the profiles with temperature, is similar for all three stoichiometries and is predicted by both models; it is also visible in the CO profiles (see Figs. 3d and S3e,f). A reaction flow analysis with both mechanisms [17,34] shows that below about 900 K, R20 is mainly responsible for O_2 consumption while R21, in contrast, may produce O_2, in this combination leading to a more gradual decrease of the profile:

$$H\dot{C}O + O_2 \rightarrow CO + H\dot{O}_2 \quad \text{(R20)},$$

$$2H\dot{O}_2 \rightarrow O_2 + H_2O_2 \quad \text{(R21)}.$$

At 950-985 K, an increased reactivity of the system is noted because R22, which consumes O_2, becomes more dominant than the O_2-producing R21:

$$\dot{H} + O_2 \rightarrow O + \dot{O}H \quad \text{(R22)}.$$

With R22, the reactive OH radical is formed leading to a stoichiometry-dependent rapid decay starting at 936 K for ϕ=0.8, 945 K for ϕ=1.0, and 953 K for ϕ=1.2. Although the *Zhao* model also represents the general profile shape of O_2, and accordingly that of CO, the *Cancino* mechanism is in most cases in better qualitative and quantitative agreement with the experimental data for all stoichiometries.

4.1.2 Hydrocarbon intermediates

Hydrocarbon intermediates including CH_4, C_2H_6, C_2H_4, and C_2H_2 are shown in Fig. 4 for ϕ=1.0 and in Fig. S4 for ϕ=0.8 and ϕ=1.2. General qualitative trends are reasonably well captured by both mechanisms. Some details are evident by closer inspection of the profiles. For example, the shape of the CH_4 profile at ϕ=1.0, presented in Fig. 4a, is in close agreement with the simulation using the *Cancino* mechanism, which predicts also the early rise of the CH_4 production already near 670 K. A similar low-temperature methane production is also seen in Fig. S4a for the lean and rich cases, again in good agreement with the *Cancino* model. The *Zhao* mechanism fails to predict this early rise completely.

Figures 4b and S4b show the profiles for C_2H_2. Note that the computed values for both mechanisms have been multiplied by 10. Both mechanisms significantly under-predict the experimental results. Acetylene is mainly formed by R23 [23,34]:

$$\dot{C}_2H_3 + O_2 \rightarrow H\dot{O}_2 + C_2H_2 \quad \text{(R23)}.$$

However, C_2H_3 is primarily consumed by the competing and dominating reaction R24 forming CH_2O:

$$\dot{C}_2H_3 + O_2 \rightarrow H\dot{C}O + CH_2O \quad \text{(R24)}.$$

It is obvious from Fig. 5a that formaldehyde is over-predicted, although to a lesser extent. Hence, one possible contribution to the underestimation of C_2H_2 may be found in the competition of R23 and R24. To better understand the discrepancies for C_2H_2, computed integrated consumption rates of C_2H_3 were analyzed. For ϕ=1.0 at 600-1000 K, R24 accounts for 50-85% of the C_2H_3 consumption, while the share of R23 is almost constant at ~10% for the *Cancino* mechanism and even lower for the *Zhao* model. In addition, another product channel forming CH_2CHO and O is involved with a share of about 20%. Thus, the competition between R23 and R24 has some influence but is unlikely the sole source of the error. Rather, there might be another direct C_2H_2 formation route that is not included in the considered kinetic models.

The general trends for C_2H_4 (Figs. 4c and S4c) and C_2H_6 (Figs. 4d and S4d) are reasonably well represented especially by the *Cancino* mechanism, which again predicts the low-temperature production of these species much better than the *Zhao* mechanism. Simulation with the latter leads to consistent shifts of the positions of the maxima to higher temperatures for all species presented in Figs. 4 and S4, typically by ~30-70 K. These shifts, if at all noted, are not as prominent for the *Cancino* mechanism where mostly only small differences are

observed in peak positions. The quantitative agreement between maximum mole fraction values in the experiment and the simulations shown in Figs. 4 and S4 is within experimental uncertainty for methane, and within less than a factor of two for both models, with the exception of acetylene. Between the two models, the difference may be larger; for example, the *Zhao* model tends to over-predict C_2H_4 and under-predict C_2H_6 for all stoichiometries, while the reverse is true for the *Cancino* model.

4.1.3 Oxygenated intermediates

Mole fraction profiles for the oxygenated intermediates CH_2O and C_2H_4O are presented in Fig. 5 for ϕ=1.0 and in Fig. S5 for the other two stoichiometries. As mentioned before, the CH_2O concentration is overestimated by both mechanisms, with one possible reason being the competition between reactions R23 and R24. A shoulder at low temperatures is consistently seen in the simulations for CH_2O with the *Cancino* mechanism, which is not as pronounced in the experiment. This feature is absent from the simulations with the *Zhao* model. The C_2H_4O signal detected in the experiment was evaluated as acetaldehyde, which was deemed to be the dominant contribution; isomer separation to detect ethenol was not possible. As seen in Fig. 5b, the species was detected over a wide range of temperatures from ~630-930 K (and similarly in the lean and rich cases shown in Fig. S5b). The gradual increase at around 630 K can be related to the respective low-temperature decrease of the fuel mole fraction. Acetaldehyde may be formed through R25 and R26 [34]:

$$CH_3CH_2OH \rightarrow CH_3CH_2\dot{O} \overset{+M0}{\rightarrow} CH_3CHO + \dot{H} + M \quad \text{(R25)},$$

$$CH_3CH_2OH \rightarrow CH_3\dot{C}HOH \overset{+O_2}{\rightarrow} CH_3CHO + H\dot{O}_2 \quad \text{(R26)}.$$

These consumption reactions of ethanol by H-abstraction leading to the isomers CH_3CH_2O and $CH_3\dot{C}HOH$ are known to be primary pathways in ethanol oxidation [17,28]. Both mechanisms, however, are not able to match the acetaldehyde formation well, potentially because ethenol contributions could be different and non-negligible along the temperature range investigated. Here, isomer-specific analysis could assist further clarification. The *Zhao* mechanism does not differentiate between different C_2H_4O species, and the *Cancino* mechanism also doesn't include ethenol. It is not clear whether ethenol formation would be significant at these low temperatures; however, minor changes to the fuel destruction reactions in the low-temperature regime might result in distinct changes of the CH_2O and CH_3CHO profiles. The prediction with the *Cancino* mechanism is again somewhat better in

the low-temperature regime, whereas the profile shape near the peak at higher temperatures is captured better by the *Zhao* mechanism.

4.2 Dimethyl ether oxidation

4.2.1 Major species

Mole fraction profiles as a function of temperature for the major species in dimethyl ether oxidation, including those for DME (fuel), O_2, H_2, CO, H_2O, and CO_2, are shown in Fig. 6 for ϕ=1.0 and in Fig. S6 for ϕ=0.8 and 1.2. The experimental results are complemented with the corresponding simulations with the *mod-CF* and *mod-Zhao* mechanisms (see Section 3.2.3). Equilibrium mole fractions calculated with the Gaseq program [68] for T=1100 K are included in these diagrams; they are offset to T>1200 K to avoid interference with measured data points. Overall, the trends are quite well predicted by both mechanisms. The measured gas composition above 1050 K is in very good agreement with the predicted thermodynamic equilibrium composition, with some deviations noted in the H_2 and CO mole fractions for the stoichiometric case, and similar but smaller deviations for these species for the fuel-rich condition.

The expected two-stage ignition in DME oxidation observed in previous experiments [32,37,48] is evident in the DME consumption profile at ϕ=1.0 with a minimum at 590 K and 26% conversion (see Fig. 6a). At temperatures above the first ignition stage, i.e. in the NTC region at ~600-800 K, the reaction rate becomes slower and the DME mole fraction rises again. This NTC region is in good agreement with previous experimental and modeling studies [32,44], which also include results at higher pressures. The simulated DME mole fraction profiles, together with the experimental data, have already been reported as the solid lines in Fig. 2a for the *mod-CF* and Fig. 2c for the *mod-Zhao* mechanisms, where they have been compared to the performance of the respective original models. Figures 6 and S6 additionally include a comparison between the two improved mechanisms with the experimental data for all major species.

For the low-temperature range of ~550-580 K, the consumption of DME is over-predicted by both mechanisms (Fig. 6a), with a minimum DME mole fraction and 52% conversion for the *mod-CF* mechanism at 557 K and a minimum at 554 K with a conversion of 64% for the *mod-Zhao* mechanism. Also, the predicted maxima are consistently found at ~30 K lower temperature than in the experiment. For all species in Figs. 6 and S6, the observed mole

fraction variations with temperature in the experiment are not as steep as in the simulations and this effect is more pronounced at lower temperature because of longer residence and thus mixing times.

With increasing temperature, the mole fraction of DME increases up to 95% of the initial mole fraction at 810 K in the *mod-CF* simulation, over-predicting the experimental data, which compare well with the *mod-Zhao* mechanism, however, where DME reaches 87% of its initial mole fraction. Complete conversion of the fuel is seen near 960 K for all three stoichiometries. The high-temperature region is well captured by both mechanisms.

Similar to the behavior discussed for ethanol oxidation (see Section 4.1.1), a change of the temperature dependence in the O_2 consumption is observed in the temperature range of 870-1010 K (Figs. 6b and S6c,d). Similar changes can be found upon closer inspection in the mole fraction profiles of CO and CO_2, especially pronounced at ϕ=1.2. A more gradual consumption of O_2 (respectively production of CO and CO_2) is noted for ϕ=1.0 above ~900 K up to ~970 K, with a steeper decrease at higher temperatures. Responsible for this behavior are again reactions R20 and R22, where R20 is the dominant reaction pathway up to ~970 K and R22 becomes more important and leads to a more rapid O_2 consumption above ~970 K.

The mole fraction profile of H_2 for ϕ=1.0, given in Fig. 6c, passes through a maximum near 970 K. According to the *mod-Zhao* model, reactions R27 and R28 are responsible for the rapid consumption of H_2 above 1000 K:

$$H_2 + \dot{O}H \rightarrow H_2O + H_2O \quad \text{(R27)},$$

$$H_2 + \dot{O} \rightarrow \dot{H} + \dot{O}H \quad \text{(R28)}.$$

A different profile shape for H_2 is seen in Fig. S6f for the fuel-rich condition, where the mole fraction rises again near 1000 K until a stable plateau is reached at ~1070 K. This high-temperature increase of the H_2 mole fraction is caused by R29 becoming dominant at these temperatures:

$$CH_4 + \dot{H} \rightarrow \dot{C}H_3 + H_2 \quad \text{(R29)}.$$

It can be concluded that both models reasonably represent all qualitative trends observed for the major species, with some deviations in quantitative values. In addition to experimental uncertainties, steeper gradients in the model may be the consequence of neglecting diffusion. No pronounced stoichiometry dependence was noted. Both models show consistent performance with over-predicting the same species, especially CO and H_2, and to some extent, also H_2O.

4.2.2 Hydrocarbon intermediates

Mole fraction profiles for hydrocarbon intermediates including CH_4, C_2H_2, C_2H_4, and C_2H_6 are shown in Fig. 7 for ϕ=1.0 and in Fig. S7 for the other two stoichiometries. The profile shapes are overall reasonably well predicted by the two mechanisms. All hydrocarbon intermediates occur predominantly in the high-temperature region above ~800 K.

Both methane and ethane profiles are well predicted (Fig.7a,d) including quantitative agreement of the maximum values with both mechanisms. A similarly good performance is also seen for ϕ=0.8 and 1.2 in Figs. S7a and S7d. The gentle slope in the ethane profile starting near 800 K is well reproduced by the *mod-Zhao* mechanism, and to a somewhat lesser degree with the *mod-CF* mechanism. In both mechanisms, ethane is completely formed through the third-body recombination reaction of two methyl radicals in the range of 750 to 950 K. At these conditions, methyl originates from the pyrolysis of CH_3OCH_2, which itself is generated by DME reacting with the hydroxyl radical. Thus, the faster DME decomposition of the *mod-Zhao* mechanism leads to the observed difference in the ethane profiles.

Mole fraction profiles for C_2H_2 and C_2H_4 are given in Figs. 7b,c and S7b,c. Note the scaling factor of 50 for the acetylene simulation results. Both models severely under-predict the C_2H_2 mole fractions. Because of this somewhat surprising observation, acetylene measurements were repeated, using also a different calibration strategy (direct calibration with cold gas sample), with good agreement with the reported results, however. Also C_2H_4 mole fractions are significantly under-predicted. In analogy to the ethanol simulations, the low C_2H_2 concentration is due to the competition between R23 and R24. For DME oxidation at stoichiometric conditions, less than 5% of C_2H_3 is converted to C_2H_2. In addition, the low mole fraction calculated for C_2H_4 contributes to the underestimation of C_2H_2, which is completely formed via C_2H_3 and C_2H_4. C_2H_4 itself is formed from C_2H_5, which originates from C_2H_6. Because no noticeable competing reaction is present in this path and mole fractions of C_2H_5 are of the order of 10^{-16}, it seems likely that increased reaction rates for the conversion of C_2H_6 to C_2H_5 and subsequently C_2H_4 are required to reach higher values for C_2H_4 as well as for C_2H_2.

The order of subsequent dehydrogenation may be inferred from the temperature at which the maximum mole fractions are found, with the sequence C_2H_6 @ 925 K < C_2H_4 @ 946 K < C_2H_2 @ 968 K for the stoichiometric case. Here, a higher temperature is equivalent to a

longer reaction time needed for the respective dehydrogenation reactions. Both models predict the same sequence.

4.2.3 Oxygenated intermediates

Mole fraction profiles of formaldehyde (CH_2O) and methyl formate (CH_3OCHO) are shown in Fig. 8 for ϕ=1.0 together with the simulations; results for the lean and rich case are presented in Fig. S8. Consistently for all three stoichiometries, formaldehyde is seen in both the low- and high-temperature regimes, while methyl formate is only present at low temperatures. The formation of these two intermediates in the low-temperature region occurs sequentially, the maximum mole fraction for CH_3OCHO at ϕ=1.0 occurs near 580 K, earlier than for CH_2O at ~600 K. Addition of molecular oxygen to the CH_3OCH_2 radical was identified as the key reaction in the low-temperature region in the *mod-Zhao* mechanism, as also reported before by several groups [32,34,48,69,70]. The resulting methoxymethylperoxy radical ($CH_3OCH_2O_2$) can react via internal H-atom transfer to the important hydroperoxy-methoxymethyl species ($CH_2OCH_2O_2H$). The methoxymethylperoxy radical is responsible for the formation of methyl formate in the low-temperature region; it can then react in different ways:

$$2\ CH_3OCH_2\dot{O}_2 \rightarrow O_2 + 2\ CH_3OCH_2\dot{O} \rightarrow CH_3OCHO + \dot{H} \quad \text{(R30)},$$

$$2\ CH_3OCH_2\dot{O}_2 \rightarrow O_2 + CH_3OCHO + CH_3OCHO \quad \text{(R31)}.$$

Both mechanisms substantially over-predict the mole fraction of methyl formate. The temperature dependence with a peak at around 550 K is actually described with reasonable accuracy, while the magnitude is over-prediced by a factor of about 20. One potential source for this disagreement might be the uncertainty in the estimated cross section for methyl formate, where more reliable data would be desirable for future work.

With increasing temperature above 600 K, the decomposition via β-scission exhibiting higher activation energy becomes gradually more dominant. Formaldehyde is formed by R32:

$$\dot{C}H_2OCH_2O_2H \rightarrow CH_2O + CH_2O + \dot{O}H \quad \text{(R32)},$$

but the reactivity of the whole system decreases. This trend is well represented by both models. Further increase of the temperature above 790 K, leads to a second maximum of the CH_2O mole fraction. At this temperature the high-temperature reaction channel becomes important where the decomposition of the fuel radical occurs predominantly through β-scission:

$$CH_3O\dot{C}H_2 \xrightarrow{\beta\text{-sc.}} CH_2O + \dot{C}H_3 \quad \text{(R33).}$$

In this temperature range, above 790 K, no methyl formate is formed because R30 and R31 are only dominant in the low-temperature region. Overall, the CH_2O mole fraction profiles are quite well captured, with a better performance of the *mod-Zhao* mechanism.

4.3 Comparison of DME with ethanol fuel

As expected, a direct comparison of the oxidation of the two isomeric C_2H_6O fuels shows a different behavior especially in the low-temperature region. DME exhibits a distinct low-temperature behavior, and its two-stage ignition has been observed in various experiments [32,37]. It is generally well described by the improved DME reaction kinetics used in this work.

Interestingly, some slow reactivity was also observed during ethanol oxidation, even though ethanol is not expected to exhibit a classical low-temperature reaction network. For example, for ethanol a slight decrease of the mole fraction beginning at low temperatures around 500-790 K is observed followed by complete conversion at 840 K, whereas the complete conversion for DME is found at an about 120 K higher temperature than for ethanol.

Another interesting feature concerns the respective dehydrogenation sequence which can be inferred from the temperatures at which the maximum mole fractions for C_2H_6, C_2H_4, and C_2H_2 are observed. While the order of subsequent dehydrogenation for DME oxidation at ϕ=1.0 is C_2H_6 @ 925 K < C_2H_4 @ 946 K < C_2H_2 @ 968 K, the order is different for ethanol oxidation under the same conditions with C_2H_4 @ 867 K < C_2H_6 @ 893 K < C_2H_2 @ 903 K. This behavior depends on the two different reaction pathways. For DME oxidation above 810 K, one main reaction channel is responsible for forming hydrocarbon intermediates, occuring via the CH_3-radical [34,38,42].

$$2\dot{C}H_3 \xrightarrow{M} C_2H_6 \rightarrow \ldots. \rightarrow C_2H_4 \rightarrow \ldots \rightarrow C_2H_2 \quad \text{(R34).}$$

In contrast, different reaction pathways are responsible in ethanol oxidation. Again, C_2H_6 can be produced from CH_3 radical recombination, and additionally C_2H_4 can be formed directly via C_2H_5OH [34,38,42].

$$\begin{array}{l} C_2H_5OH \rightarrow \dot{C}_2H_5 \\ \qquad\qquad\quad \downarrow \\ 2\,\dot{C}H_3 \xrightarrow{M} C_2H_6 \rightarrow .... \rightarrow C_2H_4 \rightarrow ... \rightarrow C_2H_2 \end{array} \quad \text{(R35).}$$

The availability of a second pathway for ethanol leads to a different order in the subsequent dehydrogenation for the two isomeric fuels. It should be noted that these dehydrogenation sequences, seen from the temperatures at which the respective maximum mole fractions occur, are well reproduced by all models for both fuels.

As already shown in Figs. 4b and 7b, the model under-predicts the experimental data for C_2H_2 by about a factor of 10 for ethanol and a factor of 50 for DME fuel. The peak mole fraction in the experiment is in the range of 10^{-5}-10^{-4} for both fuels, and the ratio between the maximum mole fractions of C_2H_2, C_2H_4 and C_2H_6 agrees well with the literature for many flow reactor and flame experiments [23,26,39,43]. To analyze this significant discrepancy in more detail, Fig. 9 presents a sensitivity analysis for C_2H_2 with the *Zhao* mechanism. The sensitivity factors are shown in Fig. 9a for DME and in Fig. 9b for ethanol, with the following reactions included for both fuels:

$$C_2H_4 + \dot{O}H \rightarrow \dot{C}_2H_3 + H_2O \quad \text{(R36)},$$

$$\dot{C}_2H_3 + O_2 \rightarrow C_2H_2 + H\dot{O}_2 \quad \text{(R37)},$$

$$H_2O_2 + M \rightarrow 2\,\dot{O}H + M \quad \text{(R38)}.$$

Furthermore the reactions

$$CH_3OCH_3 + \dot{C}H_3 \rightarrow CH_3O\dot{C}H_2 + CH_4 \quad \text{(R39)},$$

$$CH_3OCH_3 + H\dot{O}_2 \rightarrow CH_3O\dot{C}H_2 + H_2O_2 \quad \text{(R40)},$$

are also included for DME fuel. For ethanol (Fig. 9b) the following reactions are included:

$$C_2H_5OH + H\dot{O}_2 \rightarrow CH_3CHOH + H_2O_2 \quad \text{(R41)},$$

$$C_2H_5OH + H\dot{O}_2 \rightarrow C_2H_4OH + H_2O_2 \quad \text{(R42)}.$$

In both cases, R37 is the most sensitive reaction at the respective location of the peak mole fraction in the simulation results. Furthermore, hydrogen peroxide dissociation (R38) and C_2H_4 decomposition by hydroxyl radicals (R36) are relevant for both fuels at these conditions, with the latter reaction being sensitive over a larger temperature range for ethanol compared to DME. This may be the reason for the less under-predicted simulation profile of C_2H_2 for ethanol. For both fuels, reactions R39-42 involving the respective fuels are sensitive with decreasing importance for increasing temperature.

5. Summary and conclusion

The low-temperature oxidation for ethanol and dimethyl ether was investigated systematically for three different stoichiometries over a wide temperature range in a laminar flow reactor at

atmospheric pressure. Quantitative mole fraction profiles of major and intermediate species as a function of temperature were determined using a time-of-flight mass spectrometer with adequate mass resolution, coupled to the flow reactor. High-temperature resolution capable to resolve details in the oxidation chemistry was achieved by continuous ramping of the temperature. Since the experimental conditions were kept identical for both isomeric fuels, a direct comparison of the experimental results is possible.

The chemical processes in ethanol oxidation were simulated with the mechanisms of Zhao et al. [34] and Cancino et al. [17] over the entire low- and high-temperature regime. The experimental results are in general well predicted by the mechanisms. No NTC region was observed for ethanol, and the gradual ethanol consumption seen in the experiment can be understood especially from the *Cancino* mechanism, which features a number of reactions especially included for the low-temperature region and which predicts the experimental data well.

Additionally, the previously published experimental results for DME oxidation [49] were simulated, in general with good agreement, using modifications to the mechanisms of Curran et al. [32] and Fischer et al. [33] as well as of Zhao et al. [34]. The expected and observed NTC behavior of DME was well reproduced by both improved kinetic mechanisms. Also, the trends in the high-temperature region are captured well by both mechanisms.

In spite of the ability of established models to represent most general features observed in the oxidation of both fuels for a set of three pairs of conditions, there are still remarkable differences in qualitative and quantitative representation of details in profile shapes and mole fraction values for these chemically quite simple and rather well-understood fuels under these conditions. For example, it is not evident from the comparison of all experimental datasets with the available, widely validated models that one single mechanism like that of Zhao et al. [34] could simulate the oxidation for both fuels with satisfactory quality. While the *Zhao* model, with the modifications included here, performs generally better for DME oxidation, it is not well adapted to capture all relevant details in the ethanol experiment. The *Cancino* model, although it includes some additional reactions for the low- and intermediate-temperature regime leading to better general agreement with the ethanol experiments, shows remaining shortcomings in the quantitative prediction of acetylene, which are even more severe for the *Zhao* mechanism, however. Both models fail to represent the C_2H_4O profiles, a result that suggests closer consideration of ethenol versus acetaldehyde chemistry in this

temperature range. For DME oxidation, improvements would be desirable for the quantitative prediction of acetylene and methyl formate mole fractions.

Acknowledgments

The authors acknowledge generous support by Deutsche Forschungsgemeinschaft within the Collaborative Research Center SFB 686, TP B3. They further wish to thank Julia Warkentin for her assistance with the temperature measurements and Harald Waterbör for his able technical support.

References

[1] A. Dubreuil, F. Foucher, C. Mounaïm-Rousselle, G. Dayma, P. Dagaut, Proc. Combust. Inst. 31 (2007) 2879-2886.

[2] J.M. Anderlohr, A. Piperel, A. Pires da Cruz, R. Bounaceur, F. Battin-Leclerc, P. Dagaut, X. Montagne, Proc. Combust. Inst. 32 (2009) 2851-2859.

[3] S. Tanaka, F. Ayala, J.C. Keck, J.B. Heywood, Combust. Flame 132 (2003) 219-239.

[4] A. Piperel, P. Dagaut, X. Montagne, Proc. Combust. Inst. 32 (2009) 2861-2868.

[5] H. Yamada, K. Suzaki, H. Sakanashi, N. Choi, A. Tezaki, Combust. Flame 140 (2005) 24-33.

[6] A. Cavaliere, M. de Joannon, Prog. Energy Combust. Sci. 30 (2004) 329-366.

[7] M. de Joannon, A. Cavaliere, T. Faravelli, E. Ranzi, P. Sabia, A. Tregrossi, Proc. Combust. Inst. 30 (2005) 2605-2612.

[8] B.B. Dally, E. Riesmeier, N. Peters, Combust. Flame 137 (2004) 418-431.

[9] T.J. Jacobs, D.N. Assanis, Proc. Combust. Inst. 31 (2007) 2913-2920.

[10] C.A. Idicheria, L.M. Pickett, Proc. Combust. Inst. 31 (2007) 2931-2938.

[11] N. Docquier, S. Candel, Prog. Energy Combust. Sci. 28 (2002) 107-150.

[12] F. Battin-Leclerc, Prog. Energy Combust. Sci. 34 (2008) 440-498.

[13] J. Zádor, C.A. Taatjes, R.X. Fernandes, Prog. Energy Combust. Sci. 37 (2011) 371-421.

[14] N.M. Marinov, Int. J. Chem. Kinet. 31 (1999) 183-220.

[15] P. Saxena, F.A. Williams, Proc. Combust. Inst. 31 (2007) 1149-1156.

[16] O. Röhl, N. Peters, Proc. European Combustion Meeting, Vienna, Austria, 2009.

[17] L.R. Cancino, M. Fikri, A.A.M. Oliveira, C. Schulz, Energy Fuels 24 (2010) 2830-2840.

[18] L.-S. Tran, P.-A. Glaude, R. Fournet, F. Battin-Leclerc, Energy Fuels 27 (2013) 2226-2245.

[19] A. Frassoldati, T. Faravelli, E. Ranzi, K. Kohse-Höinghaus, Combust. Flame 158 (2011) 1264-1276.

[20] G. Rotzoll, J. Anal. Appl. Pyrolysis 9 (1985) 43-52.

[21] J. Li, A. Kazakov, F.L. Dryer, J. Phys. Chem. A 108 (2004) 7671-7680.

[22] T.S. Kasper, P. Oßwald, M. Kamphus, K. Kohse-Höinghaus, Combust. Flame 150 (2007) 220-231.

[23] N. Leplat, P. Dagaut, C. Togbé, J. Vandooren, Combust. Flame 158 (2011) 705-725.

[24] N. Leplat, A. Seydi, J. Vandooren, Combust. Sci. Technol. 180 (2008) 519-532.

[25] L.S. Tran, P.A. Glaude, F. Battin-Leclerc, Combust., Expl., Shock Waves. 49 (2013) 11-18.

[26] H. Xu, C. Yao, T. Yuan, K. Zhang, H. Guo, Combust. Flame 158 (2011) 1673-1681.

[27] T.S. Norton, F.L. Dryer, Int. J. Chem. Kinet. 24 (1992) 319-344.

[28] F.M. Haas, M. Chaos, F.L. Dryer, Combust. Flame 156 (2009) 2346-2350.

[29] M.U. Alzueta, J.M. Hernández, Energy Fuels 16 (2002) 166-171.

[30] P. Dagaut, C. Togbé, Energy Fuels 22 (2008) 3499-3505.

[31] H.J. Curran, W.J. Pitz, C.K. Westbrook, P. Dagaut, J.-C. Boettner, M. Cathonnet, Int. J. Chem. Kinet. 30 (1998) 229-241.

[32] H.J. Curran, S.L. Fischer, F.L. Dryer, Int. J. Chem. Kinet. 32 (2000) 741-759.

[33] S.L. Fischer, F.L. Dryer, H.J. Curran, Int. J. Chem. Kinet. 32 (2000) 713-740.

[34] Z. Zhao, M. Chaos, A. Kazakov, F.L. Dryer, Int. J. Chem. Kinet. 40 (2008) 1-18.

[35] Y. Hidaka, K. Sato, M. Yamane, Combust. Flame 123 (2000) 1-22.

[36] R. Sivaramakrishnan, J.V. Michael, A.F. Wagner, R. Dawes, A.W. Jasper, L.B. Harding, Y. Georgievskii, S.J. Klippenstein, Combust. Flame 158 (2011) 618-632.

[37] U. Pfahl, K. Fieweger, G. Adomeit, Proc. Combust. Inst. 26 (1996) 781-789.

[38] H. Xu, C. Yao, T. Yuan, K. Zhang, H. Guo, Combust. Flame 158 (2011) 1673-1681.

[39] T.A. Cool, J. Wang, N. Hansen, P.R. Westmoreland, F.L. Dryer, Z. Zhao, A. Kazakov, T. Kasper, K. Kohse-Höinghaus, Proc. Combust. Inst. 31 (2007) 285-293.

[40] Z. Chen, L. Wei, X. Gu, Z. Huang, T. Yuan, Y. Li, Z. Tian, Energy Fuels 24 (2010) 1628-1635.

[41] E.W. Kaiser, T.J. Wallington, M.D. Hurley, J. Platz, H.J. Curran, W.J. Pitz, C.K. Westbrook, J. Phys. Chem. A 104 (2000) 8194-8206.

[42] J. Wang, M. Chaos, B. Yang, T.A. Cool, F.L. Dryer, T. Kasper, N. Hansen, P. Oßwald, K. Kohse-Höinghaus, P.R. Westmoreland, Phys. Chem. Chem. Phys. 11 (2009) 1328-1339.

[43] J. Wang, U. Struckmeier, B. Yang, T.A. Cool, P. Osswald, K. Kohse-Höinghaus, T. Kasper, N. Hansen, P.R. Westmoreland, J. Phys. Chem. A 112 (2008) 9255-9265.

[44] P. Dagaut, C. Daly, J.M. Simmie, M. Cathonnet, Proc. Combust. Inst. 27 (1998) 361-369.

[45] P. Dagaut, J.-C. Boettner, M. Cathonnet, Proc. Combust. Inst. 26 (1996) 627-632.

[46] I. Liu, N.W. Cant, J.H. Bromly, F.J. Barnes, P.F. Nelson, B.S. Haynes, Chemosphere 42 (2001) 583-589.

[47] M.U. Alzueta, J. Muro, R. Bilbao, P. Glarborg, Isr. J. Chem. 39 (1999) 73-86.

[48] H. Guo, W. Sun, F.M. Haas, T. Farouk, F.L. Dryer, Y. Ju, Proc. Combust. Inst. 34 (2013) 573-581.

[49] F. Herrmann, P. Oßwald, K. Kohse-Höinghaus, Proc. Combust. Inst. 34 (2013) 771-778.

[50] P. Oßwald, H. Güldenberg, K. Kohse-Höinghaus, B. Yang, T. Yuan, F. Qi, Combust. Flame 158 (2011) 2-15.

[51] T. Kasper, P. Oßwald, U. Struckmeier, K. Kohse-Höinghaus, C.A. Taatjes, J. Wang, T.A. Cool, M.E. Law, A. Morel, P.R. Westmoreland, Combust. Flame 156 (2009) 1181-1201.

[52] P. Oßwald, K. Kohse-Höinghaus, U. Struckmeier, T. Zeuch, L. Seidel, L. Leon, F. Mauss, Z. Phys. Chem. 225 (2011) 1029-1054.

[53] H. Pitsch, FlameMaster: A C++ computer program for 0d combustion and 1d laminar flame calculations; available from http://www.stanford.edu/~hpitsch, 1998.

[54] T. Wada, A. Sudholt, H. Pitsch, N. Peters, Combust. Theor. Model., 2013, DOI:10.1080/13647830.2013.813588 .

[55] A.A. Konnov, Combust. Flame 156 (2009) 2093-2105.

[56] M.P. Dunphy, J.M. Simmie, J. Chem. Soc. Faraday Trans. 87 (1991) 1691-1696.

[57] J. Li, Experimental and numerical studies of ethanol chemical kinetics, Ph.D. Thesis, Department of Mechanical and Aerospace Engineering, Princeton University, Princeton, NJ, USA, 2004.

[58] J. Li, A. Kazakov, M. Chaos, F.L. Dryer, Proc. 5th National US Combustion Meeting, San Diego, California, USA 2007.

[59] K.A. Heufer, H. Olivier, Shock Waves 20 (2010) 307-316.

[60] L.F. Loucks, K.J. Laidler, Can. J. Chem. 45 (1967) 2763-2766.

[61] K. Schofield, Prog. Energy Combust. Sci. 34 (2008) 330-350.

[62] K. Schofield, Energy Fuels 26 (2012) 5468-5480.

[63] R.S. Tranter, P.T. Lynch, C.J. Annesly, J. Phys. Chem. A 116 (2012) 7287-7292.

[64] D.L. Baulch, C.J. Cobos, R.A. Cox, C. Esser, P. Frank, Th. Just, J.A. Kerr, M.J. Pilling, J. Troe, R.W. Walker, J. Warnatz, J. Phys. Chem. Ref. Data 21 (1992) 411-734.

[65] W. Tsang, R.F. Hampson, J. Phys. Chem. Ref. Data. 15 (1986) 1087-1279.

[66] E.L. Petersen, D.M. Kalitan, S. Simmons, G. Bourque, H.J. Curran, J.M. Simmie, Proc. Combust. Inst. 31 (2007) 447-454.

[67] M. Page, M.C. Lin, Y. He, T.K. Choudhury, J. Phys. Chem. 93 (1989) 4404-4408.

[68] C. Morley, Gaseq: Chemical Equilibria in Perfect Gases (Version 0.79). Available from http://www.gaseq.co.uk2006.

[69] A. Andersen, E.A. Carter, Isr. J. Chem. 42 (2002) 245-260.

[70] A. Andersen, E.A. Carter, J. Phys. Chem. A 107 (2003) 9463-9478.

Table 1: Conditions for the oxidation of DME and ethanol.

	Stoichiometry		
	0.8	**1.0**	**1.2**
fuel [g/min]	0.0066	0.0078	0.0088
O_2 [g/min]	0.0168	0.0161	0.0153
Ar [g/min]	0.864	0.864	0.864
Total gas flux [g/min]	0.8877	0.8882	0.8884

Table 2: Original [33] and modified [34] reaction rate expressions for the updated reactions R5, R6, and R7 in the *CF* mechanism [32,33], given in the form $A \times T^n \times e^{(-E/RT)}$. For comparison, the values of the rate coefficient *k* at 828 K are included.

Reaction		**Ref.**	**A** ($cm^3\ mol^{-1}\ s^{-1}$)	**n**	**E** ($kJ\ mol^{-1}$)	**k at 828 K** ($cm^3\ mol^{-1}\ s^{-1}$)
R5	Original	[33]	1.445E-06	5.730	23.845	2.38E+09
	Modified	[34]	2.680E+01	3.778	40.297	8.13E+09
R6	Original	[33,60]	1.600E+13	0.000	106.692	2.98E+06
	Modified	[34]	1.200E+13	0.000	107.738	1.92E+06
R7	Original	[32,33]	2.000E+16	0.000	169.452	4.09E+05
	Modified	[34]	3.000E+16	0.000	167.360	8.31E+05

Table 3: Modified reaction rate expressions [32,33] for the updated reactions R12-R16 in the Zhao et al. [34] mechanism and original rate expression for R16, given in the form $A \times T^{n} \times e^{(-E/RT)}$.

Reaction		**Ref.**	**A** ($cm^3\ mol^{-1}\ s^{-1}$)	**n**	**E** ($kJ\ mol^{-1}$)
R12	Modified	[32,33,64]	4.343E+27	-3.420	127.486
R13	Modified	[32,33,65]	1.990E+12	0.000	48.827
R14	Modified	[32,33,66]	1.000E+13	0.000	-5.02
R15	Modified	[31,32,33]	1.680E+13	0.000	74.015
R16	Original	[34,67]	8.300E+17	-1.2	64.852
	Modified*	[32,33,67]	5.450E+13	0.000	56.484
	Low-pressure limit		2.340E+25	-2.700	128.030

***** Both rate expressions for R16, in "original" and "modified" form, were reported by Page et al. [67]. In the *CF* mechanism [32,33] and the *Zhao* mechanism [34], different values specifically for the pressure dependence were selected.

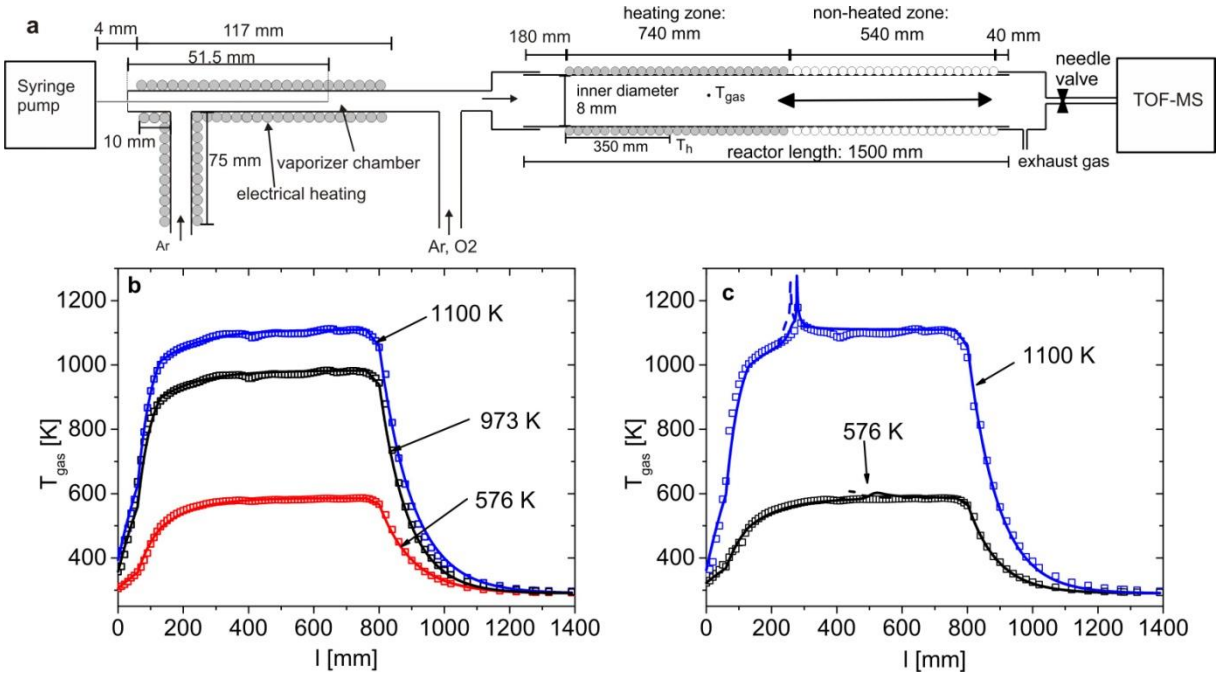

Figure 1: ***a)*** Schematic drawing of the vaporizer system and the flow reactor. ***b)*** Temperature profiles for 0.5 slm Ar for isothermal conditions; *symbols:* experiment; *lines:* simulation. ***c)*** Temperature profiles for stoichiometric DME oxidation, with Ar diluent of 97% at 0.5 slm for two different heating temperatures T_h; *symbols:* experiment; *lines:* simulation; *solid: CF* mechanism; *dashed: Zhao* mechanism.

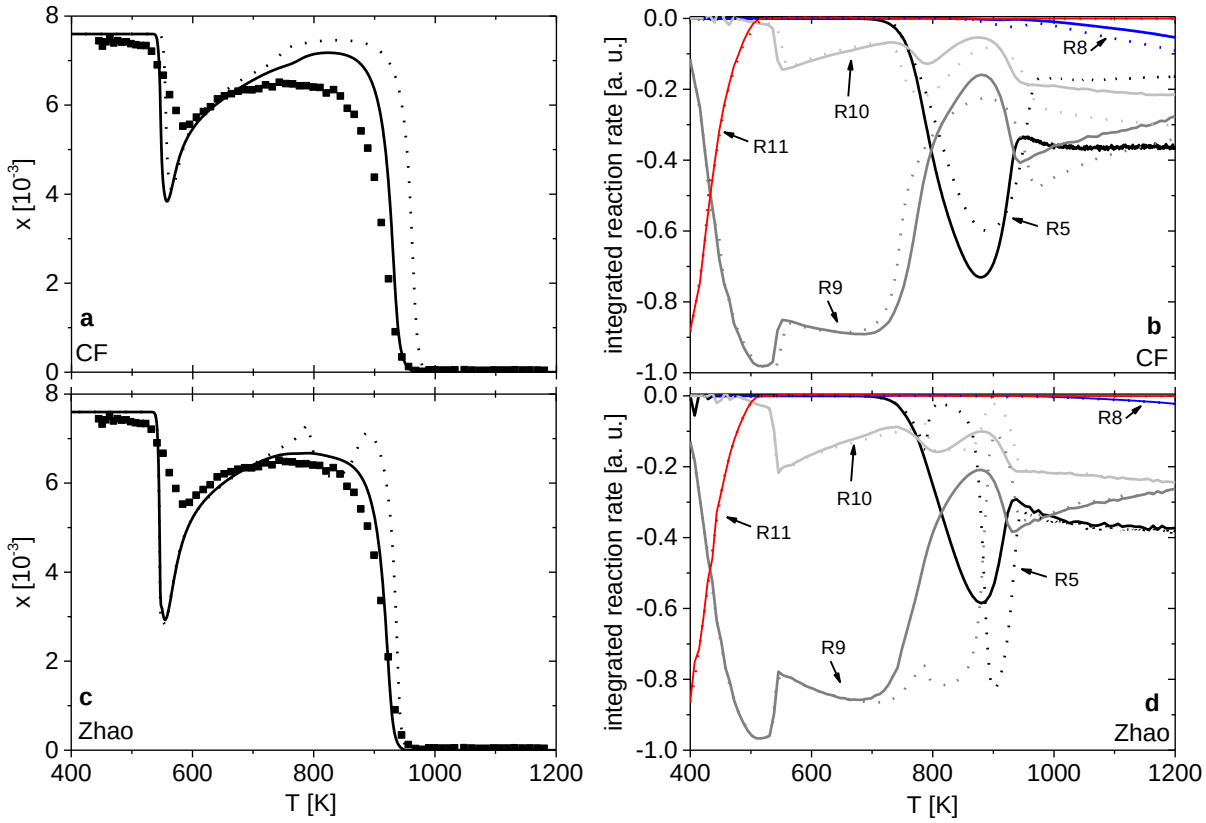

Figure 2: Mole fractions of DME (a,c) and normalized integrated reaction rates (b,d) for DME oxidation at stoichiometric conditions. *Symbols:* experiment; *solid lines:* modified models; *dashed lines:* original models; *CF:* Curran et al. / Fischer et al. mechanism [32,33]; *Zhao:* mechanism by Zhao et al. [34].

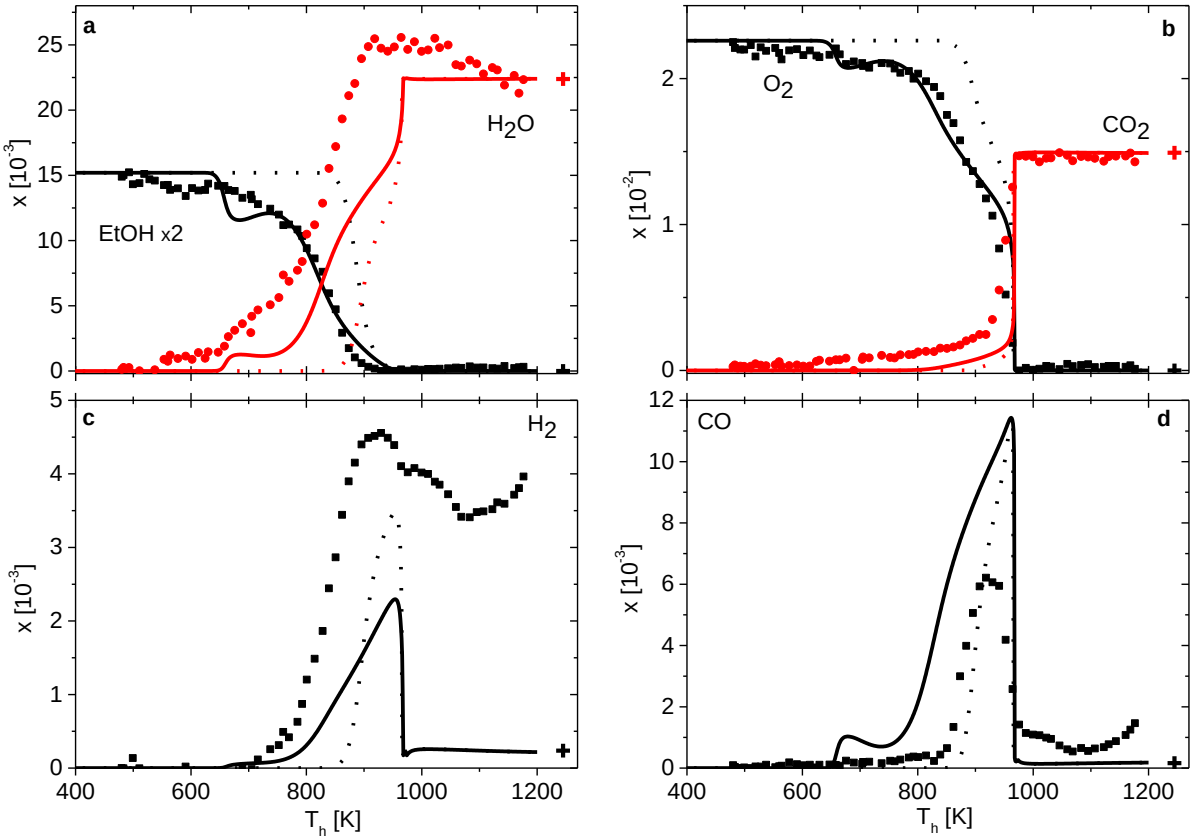

Figure 3: Major species mole fractions in ethanol oxidation as a function of temperature at ϕ=1.0. *Symbols:* experiment; *lines:* simulation; *dashed*: *Zhao* mechanism; *solid: Cancino* mechanism.

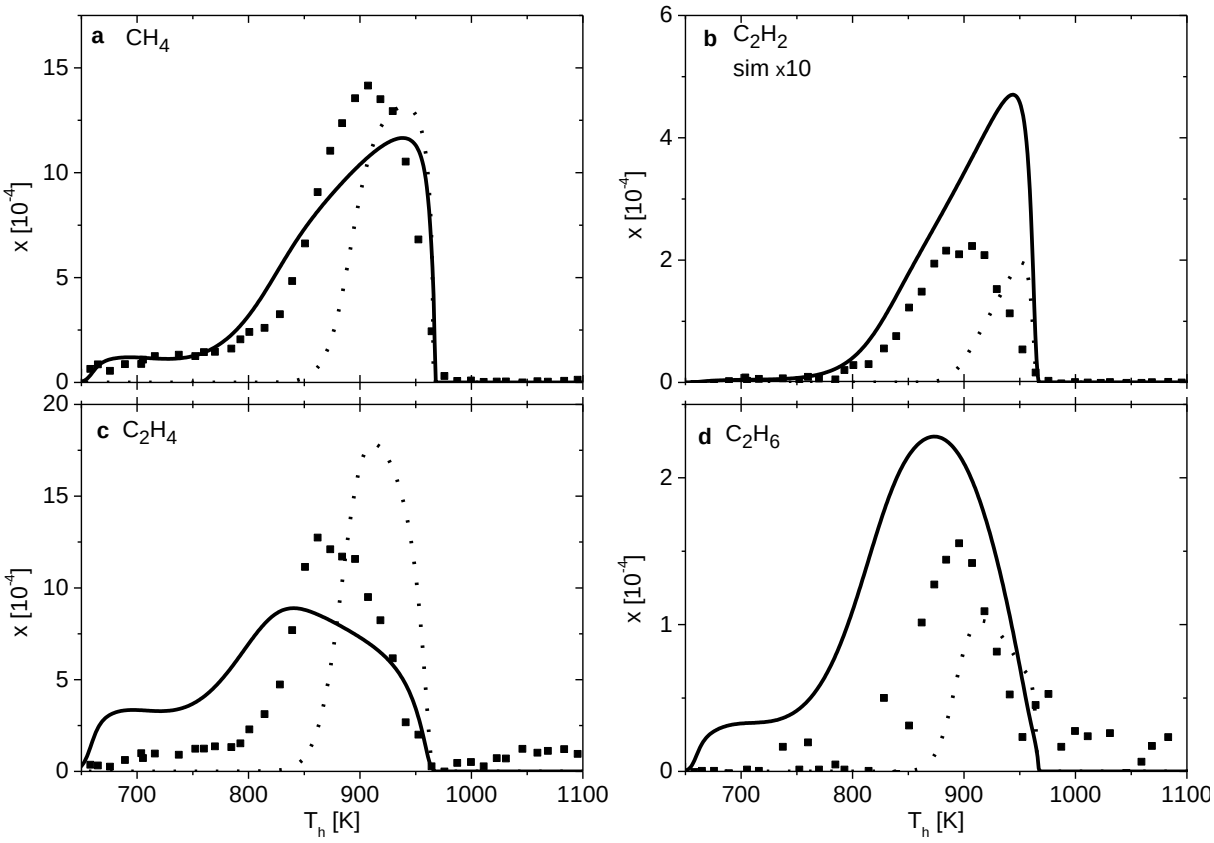

Figure 4: Mole fractions of hydrocarbon intermediates in ethanol oxidation as a function of temperature at ϕ=1.0. *Symbols:* experiment; *lines:* simulation; *dashed*: *Zhao* mechanism; *solid: Cancino* mechanism.

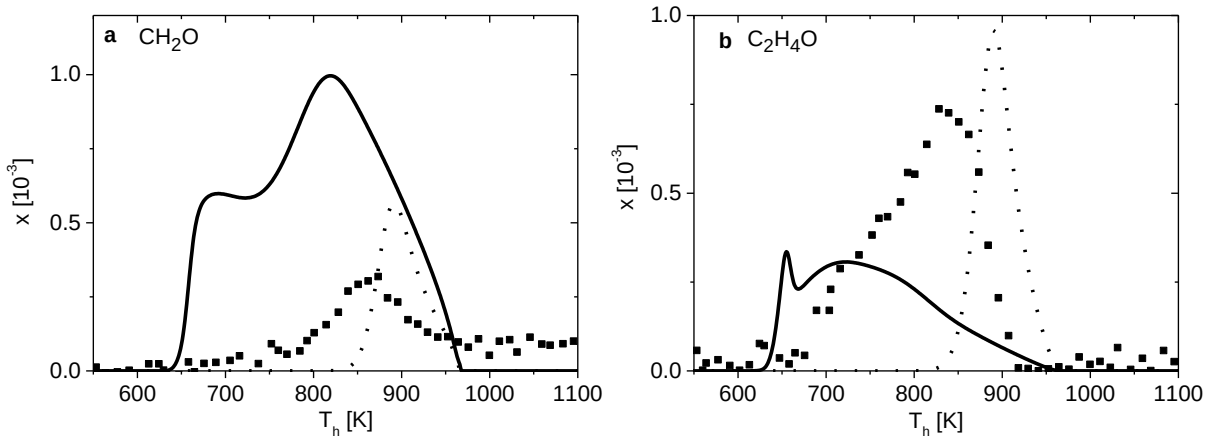

Figure 5: Mole fractions of oxygenated intermediates in ethanol oxidation as a function of temperature at ϕ=1.0. *Symbols:* experiment; *lines:* simulation; *dashed*: *Zhao* mechanism; *solid: Cancino* mechanism.

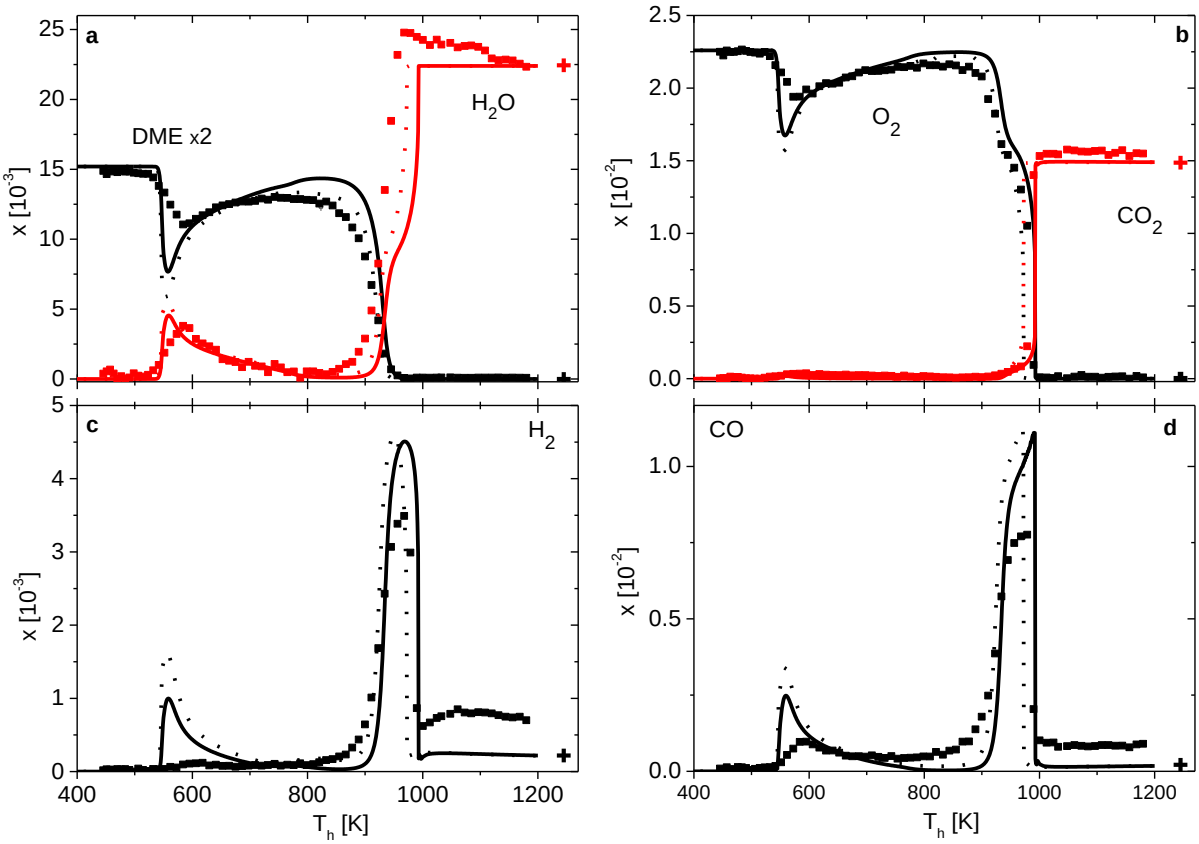

Figure 6: Major species mole fractions in DME oxidation as a function of temperature at ϕ=1.0. *Symbols:* experiment; *lines:* simulation; *dashed: mod-Zhao* mechanism; *solid: mod-CF* mechanism.

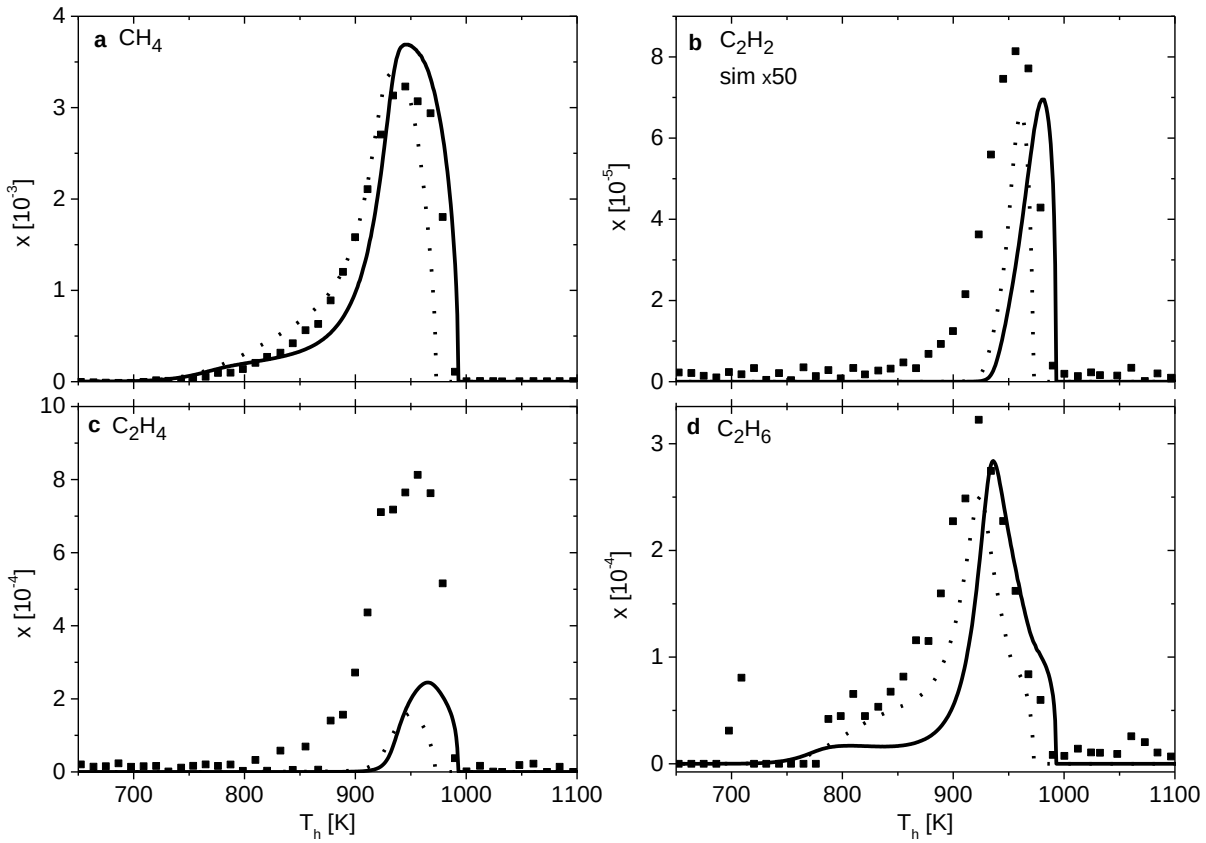

Figure 7: Mole fractions of hydrocarbon intermediates in DME oxidation as a function of temperature at ϕ=1.0. *Symbols:* experiment; *lines:* simulation; *dashed: mod-Zhao* mechanism; *solid: mod-CF* mechanism.

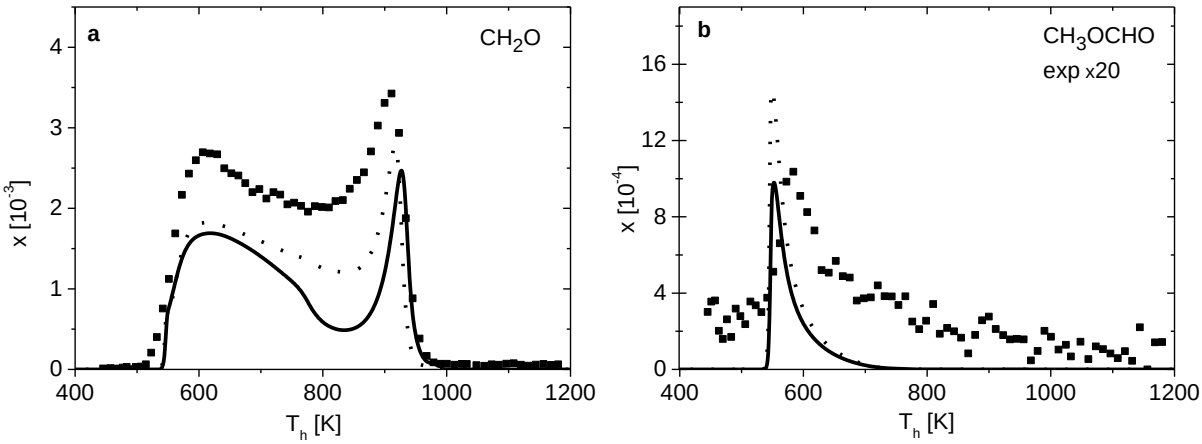

Figure 8: Mole fractions of oxygenated intermediates in DME oxidation as a function of temperature at ϕ=1.0. *Symbols:* experiment; *lines:* simulation; *dashed: mod-Zhao* mechanism; *solid: mod-CF* mechanism.

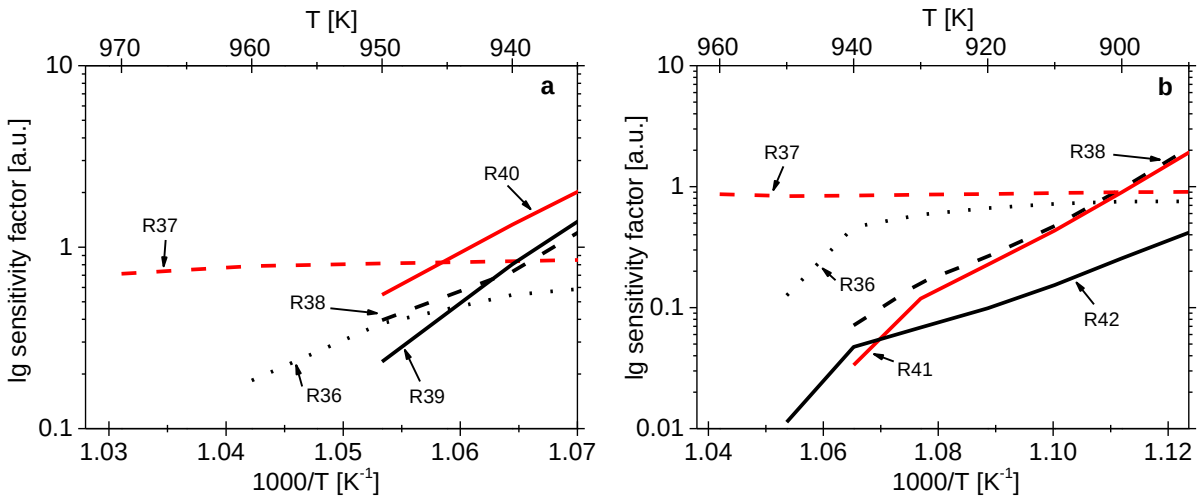

Figure 9: Sensitivity factors for dimethyl ether (a) and ethanol (b) oxidation at stoichiometric conditions.